


Percolation through voids around toroidal inclusions

A. Ballow, P. Linton, and D. J. Priour, Jr. 

Department of Physics and Astronomy, Youngstown State University, Youngstown, Ohio 44555, USA



(Received 23 August 2022; accepted 4 January 2023; published 27 January 2023)

In the case of media comprised of impermeable particles, fluid flows through voids around impenetrable grains. For sufficiently low concentrations of the latter, spaces around grains join to allow transport on macroscopic scales, whereas greater impenetrable inclusion densities disrupt void networks and block macroscopic fluid flow. A critical grain concentration ρ_c marks the percolation transition or phase boundary separating these two regimes. With a dynamical infiltration technique in which virtual tracer particles explore void spaces, we calculate critical grain concentrations for randomly placed interpenetrating impermeable toroidal inclusions; the latter consist of surfaces of revolution with circular and square cross sections. In this manner, we study continuum percolation transitions involving nonconvex grains. As the radius of revolution increases relative to the length scale of the torus cross section, the tori develop a central hole, a topological transition accompanied by a cusp in the critical porosity fraction for percolation. With a further increase in the radius of revolution, as constituent grains become more ringlike in appearance, we find that the critical porosity fraction converges to that of high-aspect-ratio cylindrical counterparts only for randomly oriented grains.

DOI: [10.1103/PhysRevE.107.014902](https://doi.org/10.1103/PhysRevE.107.014902)

I. INTRODUCTION

Fluid flow and charge transport in porous media are of practical and fundamental importance in a variety of settings. In the case of materials comprised of impermeable grains, fluid flow is through irregularly shaped void spaces surrounding the impenetrable particles rather than through well delineated channels. The concentration of the constituent grains determines the degree of fluid flow or charge transport in the medium. With increasing volume density ρ (i.e., where $\rho = N/V$) of impermeable barrier particles, void regions among grains are more likely to be smaller truncated volumes with no access to the rest of the system. Bulk level transport ultimately ceases beyond a critical concentration ρ_c . The shift from system spanning void networks admitting fluid flow on a macroscopic scale to isolated volumes whose finite size precludes bulk permeability is a percolation transition, a genuine second-order phase transition with all of the concomitant hallmarks and singular behavior [1]. The percolation threshold is customarily specified with $\eta_c = \rho_c v_B$ and $\phi_c = e^{-\eta_c}$ (v_B being the volume of the interpenetrating grains), with ϕ_c the critical porosity fraction.

Discrete percolation phenomena as well as continuum percolation involving overlapping particles are amenable to a variety of techniques such as the Hoshen-Kopelman algorithm [2] for identifying connected clusters and thereby determining if a system percolates. However, while the flow of fluid through spaces between inclusions offers a natural way to describe percolation phenomena for porous materials made up of impenetrable grains, the geometry of networks of connected voids is in general difficult to anticipate *a priori*.

Void percolation transitions have previously been studied in the context of interpenetrating particles with a variety of geometries. Due to the high degree of symmetry,

determining if assemblies of randomly placed spheres contain system spanning contiguous void volumes (and therefore if the disorder realization percolates) is amenable to Voronoi tessellation [3–6]. More generally, extrapolation to the continuum limit of discretized systems with an ever finer mesh has been used in the case of randomly placed spheres [7,8], ellipsoids [9,10], and aligned cubes [11]. For a geometrically exact approach applicable to a broader range of grain shapes, we use virtual tracer particles to dynamically infiltrate void spaces, where interactions with grains involve specular reflections off of the surfaces of impermeable inclusions. Dynamical simulations in this fashion have been reported previously in the context of randomly placed spheres [12–17] and for the case of convex solids such as the platonic solids, cylinders, cones, and ellipsoids [18]. For a computationally efficient large-scale treatment, we report on simulations in which virtual tracer particles begin their journeys at the center of a large cubic assembly of grains, with linear trajectories interrupted by collisions with and specular reflection from the surfaces of impenetrable inclusions (i.e., as in the Lorentz gas model [12,19–22]).

Common to previous studies of void percolation phenomena is the convexity of constituent grains. In this work we calculate percolation thresholds and study critical behavior for situations in which the impermeable particles are nonconvex. In particular, we consider percolation phenomena involving torus-shaped grains bounded by surfaces of revolution about an axis of symmetry (i.e., tori with square and circular cross sections). Moreover, in this work we examine porous media made up of randomly oriented inclusions as well as assemblies of tori with their axes of symmetry aligned. In addition to the novelty inherent in their manifestly nonconvex geometry, the study of toroidal grains offers the opportunity to examine how void percolation is influenced by the change in topology as the

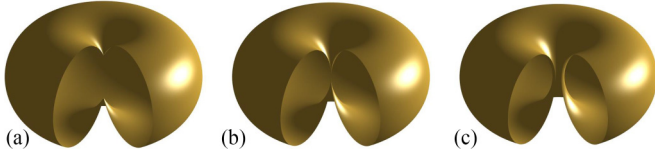


FIG. 1. Cutaway view of tori of circular cross section with (a) $\tilde{r}_1 = 0.47$, (b) $\tilde{r}_1 = 0.5$, and (c) $\tilde{r}_1 = 0.53$.

genus increases from zero to one. This transition is marked by the appearance of a central hole as solid cylinders become annular cylinders for tori with square cross sections while a symmetrically placed pair of cone-shaped indentations on a spheroidal surface above and below the equatorial plane merge and yield a doughnut shape for tori with circular cross sections as illustrated in Fig. 1. In the case of the latter, when grains are randomly oriented, singular behavior in the form of a cusp in the critical porosity fraction ϕ_c accompanies the appearance of a central hole. We find that ϕ_c then sharply decreases beyond this geometric shift as broadening central channels provide additional connections among void volumes. Examples of porous media considered in this work appear in Fig. 2 for toroidal grains of circular cross section and in Figs. 3(a) and 3(b) for tori of square cross section. Linear counterparts for the former and latter include cylinders and square prisms [e.g., as shown Figs. 3(c) and 3(d)]. Although critical porosity fractions for cylinders have been reported on previously [18], here we calculate percolation thresholds for voids surrounding randomly placed square prisms.

We label the regime in which the radius of revolution is very large relative to the cross-section diameter or width as the high-aspect-ratio limit since cutting and distorting the ringlike

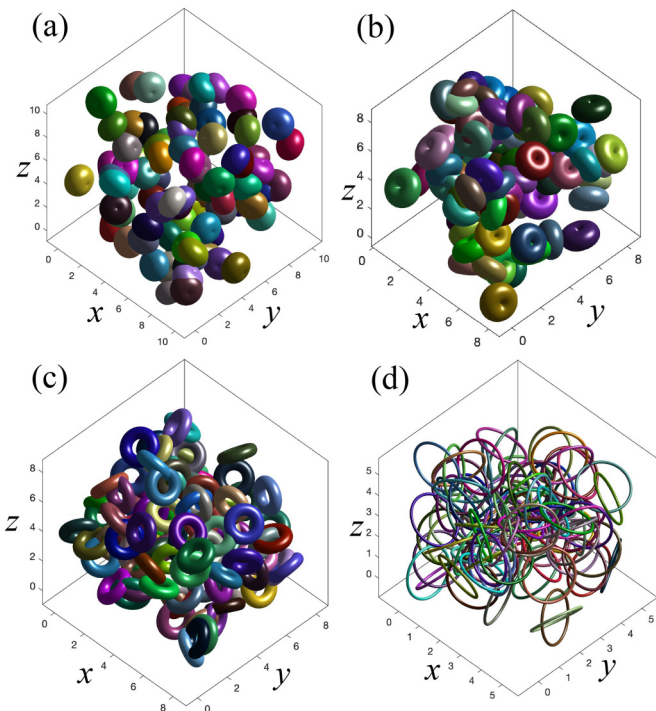


FIG. 2. Randomly oriented tori for aspect ratios (a) $\tilde{r}_1 = 0.30$, (b) $\tilde{r}_1 = 0.50$, (c) $\tilde{r}_1 = 0.70$, and (d) $\tilde{r}_1 = 0.95$.

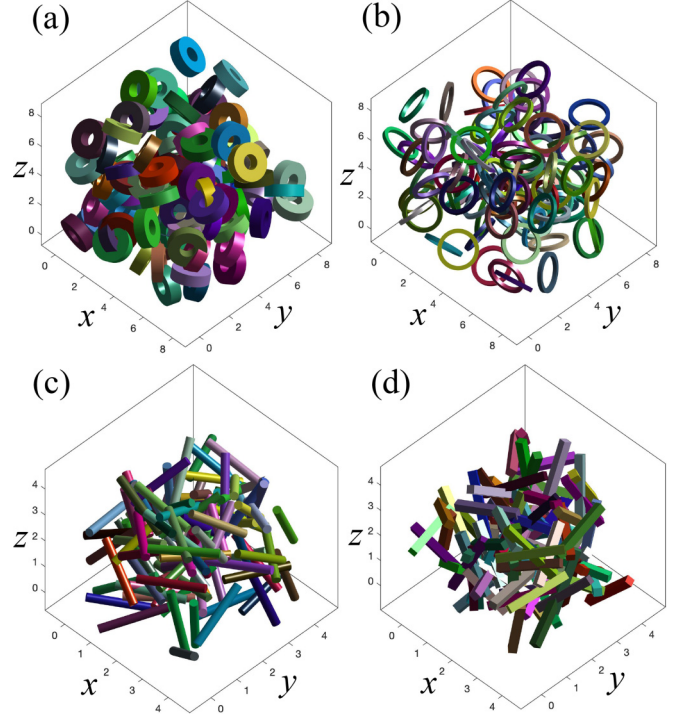


FIG. 3. Randomly oriented tori of square cross section for (a) $r_1^* = 0.70$, (b) $r_1^* = 0.90$, (c) cylinders for $r_A = 8$, and (d) square prisms for $r_A = 8$.

toroidal grains into a linear shape yields very narrow square prisms or cylinders in this regime. For the sake of a direct comparison, we define the aspect ratio r_A for cylinders and square prisms to be the ratio of the length to the diameter or square side width. On the other hand, in the case of tori, one has $r_A = \pi r_1/r_2$, or the ratio of the circumference of the circle of revolution made up of the centers of the shapes of revolution to the cross-section diameter or width, as appropriate. We calculate percolation thresholds for aligned and randomly oriented high-aspect-ratio toroidal grains as well as for the linear counterparts, finding a convergence of critical porosity fractions to a finite value. That small segments of high-aspect-ratio tori resemble their linear counterparts suggests at least the possibility that their ϕ_c values tend to a common critical porosity fraction in this regime; we find that this occurs only in the case of randomly oriented grains, while ϕ_c for tori with their axes of symmetry aligned is significantly higher than that of aligned linear counterparts in this limit. In the case of the latter, the discrepancy is likely due to at least in part to the fact that in spite of the alignment of the axes of symmetry, the random orientation of small quasilinear segments of neighboring ringlike tori in the torus equatorial plane precludes the presence of long channels among aligned linear shapes such as square prisms or cylinders of circular cross section that would otherwise facilitate fluid flow on macroscopic scales.

II. METHODS AND TECHNIQUES

A. Overview

Single-parameter finite-size-scaling analysis has historically been an important tool in the study of critical behavior

in percolating systems and continuous phase transitions more broadly. In this framework, finite-size effects facilitate rather than impede extrapolation to the thermodynamic limit, and central to the analysis is the scaling form $F(L, \rho) = L^{A/\nu} g[L^{1/\nu}(\rho - \rho_c)]$, where F is a thermodynamic observable, g is a universal scaling function, L is the system size, and A and ν are critical exponents associated with F and the correlation length ξ , respectively. This scaling analysis on a spatial domain draws on knowledge of void networks not often readily available, and for this reason we operate instead on the temporal domain; we calculate time-dependent observables such as the root-mean-square (rms) displacement δ_{rms} from a randomly selected interstitial point at the center of a large cube-shaped simulation volume. We consider a scaling form $\delta_{\text{rms}}(\rho, t) = t^k r[t^x(\rho - \rho_c)]$ [1,23], where $k = 1/d'_w$ and $x = 1/d_w$ are anomalous diffusion exponents for unrestricted motion averaged over all void networks for k and diffusion only through system spanning void clusters for x . Here d'_w and d_w are fractal dimensions of the former and latter random walks [1,23]; $r(y)$, where $y \equiv t^x(\rho - \rho_c)$, is a scaling function. Universal scaling arguments yield $k = (\nu - \beta/2)/(2\nu + \mu - \beta)$ and $x = 1/(2\nu + \mu - \beta)$, where $\nu = 0.8764(12)$ [24], $\beta = 0.418\,10(57)$ [24], and μ are universal critical exponents for percolation phase transitions. Although the dynamical exponents k and x may deviate from their discrete lattice counterparts $k_{\text{lat}} = 0.2001(7)$ and $x_{\text{lat}} = 0.2998(4)$ [obtained using $\mu_{\text{lat}} = 2.0009(10)$ [25]], universality theoretical arguments posit that $k/x = \nu - \beta/2 = 0.667(1)$.

B. Dynamical infiltration

To implement the diffusive exploration of void networks, we use a geometrically exact dynamical infiltration technique in which virtual tracer particles follow linear paths and interact with impenetrable inclusions via specular reflections. This approach, validated in the context of porous media comprised of a variety of convex grain shapes, also has the advantage of requiring only information local to the path of the tracers, allowing access to larger system sizes while permitting a computationally efficient approach. The principal observable we calculate is δ_{rms} , the rms displacement from the start of the tracer trajectory. The latter encompasses on average at least 10^7 scattering events from impermeable grains, and we consider 50 000 disorder realizations for each inclusion concentration we sample. To optimize computational efficiency, in terms of both the speed of the calculations and memory usage, we subdivide the simulation volume into cube-shaped voxels (similar to Verlet cells [20]). The virtual tracers propagate along their linear trajectories given by $\vec{x} = \vec{x}_0 + \hat{v}t$, with \vec{x}_0 the starting point and $|\hat{v}| = 1$ for the (unit) velocity magnitude until either reaching the nearest voxel wall or colliding with a grain, whichever is closest. In the event of the latter, specular reflection is implemented and the virtual tracer trajectory resumes with a new velocity $\hat{v}_{\text{new}} = \hat{v}_{\text{old}} - 2(\hat{v}_{\text{old}} \cdot \hat{n}_{\text{loc}})\hat{n}_{\text{loc}}$, where \hat{n}_{loc} is the local (unit) normal direction at the intersection point and \hat{v}_{old} is the previous velocity. The identical total dwell time for each trajectory (i.e., equal to the tracer path length since $|\hat{v}| = 1$) is of sufficient duration to encompass on average at least 10^7 interactions of tracers with grains.

An overall rescaling of the simulation volume and its contents has no impact on the status of the system with respect to percolation since $\eta = \rho v_B$ remains constant. Nonetheless, in practical terms, a change in the relative size of grains and the voxels is consequential due to the effect on the computational burden of propagation of tracers through the void network. If the impermeable inclusions are too small relative to the voxels, the large number of grains contained or shared by cubic cells erodes the advantage of dividing the system into smaller subvolumes. However, this circumstance may be mitigated with a dilation of the size of the system and its contents with the voxel edge length held constant; with the number density ρ decreasing, the mean number of inclusions encompassed in or sharing cubic cells decreases. In the other extreme, with voxels dwarfed by very large grains, the benefit of having very few grains overlap a cube-shaped cell is offset by the small distances traversed by virtual tracer particles as they travel from one cubic cell to the next. Rescaling the grains while the voxel dimensions (with unit edge lengths) remain fixed, across the range of geometries and aspect ratios we consider, we find computational efficiency to be optimized when on average on the order of a dozen inclusions overlap with a voxel.

It is computationally expedient to consider spheres circumscribed about inclusions, since in checking for interactions with impermeable inclusions, many candidates are eliminated with a comparatively small computational investment if spheres circumscribing the grain are not penetrated by tracer trajectories, with the task of finding intersections with the geometrically more intricate inclusions themselves reserved for the small share of candidates not ruled out in this manner. In addition, the sphere radius r_s is comparable to the grain's dominant length scale and thus serves as a dilation factor, scaled up from unity as needed to keep the number of grains in contact with a voxel on the order of a dozen.

We operate in the vicinity of the percolation transition where system spanning void networks encompass only a small fraction of the total interstitial volume in the porous medium, of which an even smaller subvolume is explored by virtual tracers. A typical case with only voxels visited by tracer particles highlighted (small red cubes) is shown in Fig. 4, where the large green cube indicates the simulation volume as a whole. The fact that tracer particles only infiltrate a small portion of the simulation volume presents an opportunity to reap a significant computational advantage, which we exploit by only requiring that voxels visited by the tracers and neighboring cells (i.e., voxels which in principle could contain a grain in contact with the cell occupied by the tracer) be populated with randomly placed impermeable inclusions.

The manner in which voxels are populated differs depending on whether the cell is invaded by a virtual tracer or is neighbor to a voxel entered by a tracer particle. Voxels are deemed blank until impermeable grains are introduced by rigorously sampling Poissonian statistics which can be achieved with a lookup table in conjunction with stochastic input. In this vein, one considers a cubic cell subdivided into N subvolumes V/N , where V is the voxel volume. The probability of strictly zero grain occupancy $P_0 \approx (1 - \rho V/N)^N$ tends to $P_0 = e^{-\rho V}$ in the continuum limit; similar logic for exactly m inclusions yields $P_m = (\rho V)^m e^{-\rho V} / m!$, with $m!$ being a combinatorial factor. Since $\sum_{m=1}^{\infty} P_m = 1$, these probabilities

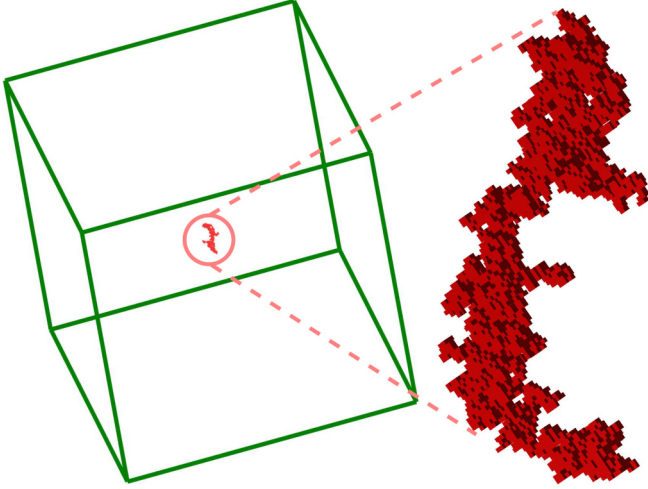


FIG. 4. Voxels visited by tracer particles shown in red for 10^7 interactions of virtual tracers with tori of circular cross section for $\tilde{r}_1 = 0.70$. Small red cubes are voxels visited by tracer particles; the simulation volume is indicated by the large green cube.

cumulatively span the unit interval, with the voxel occupancy conveniently and objectively determined with random numbers sampled uniformly over the interval $[0,1]$.

If a virtual tracer enters a blank cell, then it and each of the neighboring voxels are populated with inclusions if the latter are blank. Subsequently, all grains in contact with the cell occupied by the tracer particle are identified (along with those in the cell itself) in the event that the tracer returns to the same cell as frequently occurs. On the other hand, if a virtual tracer enters a voxel previously occupied as a neighboring cell, one need only populate blank cells which neighbor it with randomly placed grains and identify inclusions in contact with the voxel. Operating in this way with a suitable rescaling of the grain dimensions significantly improves computational efficiency, particularly in the high-aspect-ratio regime, while also reducing memory usage to the degree that we consider in this work cubic simulation volumes 1000 unit lengths on a side and containing 10^9 voxels (each in contact with on the order of a dozen inclusions) in total. For all geometries considered and with trajectories encompassing at least on the order of 10^7 collisions with grains, no tracers have exited the simulation volume, which is effectively infinite for our purposes.

In this work we calculate percolation thresholds and study critical behavior for tori with circular and square cross sections. For the latter, we also report results for the linear counterpart, square prisms; critical porosity fractions for cylinders with circular cross sections have been previously calculated [18]. Finding intersections of tracer trajectories with candidate impermeable grains and identifying neighboring grains in contact with a cube-shaped voxel draws on details of the inclusion geometry. Virtual tracers diffusing through void networks interact with the nearest impermeable inclusion, tantamount to finding the minimum travel time for the trajectory $\vec{x} = \vec{x}_0 + \hat{v}t$.

In the case of square prisms, one need only check for intersections with each of the six planar facets, subject to the

constraint that the intersection point is interior with respect to the planes containing the five remaining facets. Finding intersections of tracer trajectories with nonconvex grains such as the toroidal inclusions we consider in this work is geometrically more subtle. The randomly placed toroidal inclusions we consider in this study are uniquely characterized by the orientation of their axis of symmetry, the location of their geometric center, and the length scales r_1 and r_2 . For tori with square and circular cross sections, r_2 is the cross-section radius for the latter and half the edge length of the square cross section for the former, while r_1 is the radius of revolution in both cases. It is convenient to specify the shape of tori of circular cross section in terms of the dimensionless variable $\tilde{r}_1 = r_1/(r_1 + r_2)$, where $\tilde{r}_1 = 0$ corresponds to spherical grains, while $\tilde{r}_1 = 1$ is the high-aspect-ratio ring-like limit for inclusions and $\tilde{r}_1 = 0.50$ marks the topological transition where the central hole appears with increasing \tilde{r}_1 . Similarly, in the case of tori of square cross section we use $r_1^* = r_1/r_s$, where r_s is the radius of the circumscribed sphere, or $r_1^* = 1/\sqrt{1 + (r_2/r_1) + (r_2/r_1)^2}$. As in the case of tori of circular cross section, the extreme ringlike limit is attained as one approaches $r_1^* = 1$, while a cylindrical central channel emerges for $r_1^* = 1/\sqrt{5}$.

As nonconvex objects, toroidal inclusions allow for the possibility of multiple specular reflections from the same grain, an element of the tracer dynamics which must be taken into consideration for tori of both circular and square cross sections. The former are annular cylinders with an upper and a lower planar surface and inner and outer curved surfaces. Only tracers scattered from the inner boundary may interact in immediate succession with the same inclusion, bouncing off the wall of the central hole until emerging from the cylindrical channel. On the other hand, tori with circular cross sections are bounded by a single smooth surface and the tracer path may cross the torus as many as four times or may avoid contact with it altogether. As discussed in the Appendix, this circumstance is unsurprising given that solving for t involves solving a quartic equation, which one may do analytically. In the event that a tracer trajectory passes through a grain, the point of contact is the nearest intersection corresponding to the smallest value of t .

Essential to the very modest scaling of the computational burden (given an optimal choice of the dilation factor r_s) with the grain aspect ratio is finding which inclusions in neighboring voxels share the volume of the cell occupied by the tracer. In the case of square prisms, one checks if any of the eight prism vertices are interior to the voxel and vice versa for the cell vertices and the prism interior, which would indicate overlap among the voxel and the inclusion. Similarly, edge segments of either polyhedron penetrating the interior of the other also indicate contact among the cell and the prism-shaped grain.

For inclusions with toroidal geometry, a straightforward and tractable way to check for overlap with a voxel is to circumscribe the cubic cell with a sphere and check for overlap among the sphere and the toroidal inclusions. For this purpose, one operates in a coordinate system with the torus geometric center at the origin and the z axis aligned with the grain's axis of symmetry. One then chooses the x axis such that the

xz plane bisects the sphere circumscribed about the voxel. In this manner, determining if the sphere and the torus overlap is reduced to the task of checking to see if a circle overlaps two squares or two circles for tori with square and circular cross sections, respectively.

To calculate the percolation thresholds and study critical behavior, we conduct dynamical infiltration simulations for grain densities ρ in the vicinity of ρ_c . Dwell times for virtual tracers are such that tracers interact with impermeable inclusions at least 10^7 times on average. Critical concentration results obtained in this manner are in accord with an independent set of simulations for a mean number of collisions (10^6) an order of magnitude lower.

C. Single-parameter temporal scaling analysis

As noted previously, finite-size-scaling analysis in the spatial domain for a generic observable F , near ρ_c posits a form $F(\rho, L) = L^{A/\nu} g[L^{1/\nu}(\rho - \rho_c)]$, where A is the scaling exponent for G at ρ_c , ν is the correlation length exponent, and g is a universal scaling function. Due to this scaling form, plotting $L^{-\alpha/\nu} F$ with respect to $t \equiv L^{1/\nu}(\rho - \rho_c)$ would in principle yield a data collapse and an avenue for finding the critical indices α , ν , and ρ_c . In a very similar spirit, we use a scaling analysis with respect to time, we envisage a scaling form $\delta_{\text{rms}} = t^k r[t^x(\rho - \rho_c)]$, and we again benefit from the data collapse phenomenon in which Monte Carlo data in principle fall on a single curve when plotted with respect to $y = t^x(\rho - \rho_c)$ [i.e., the argument of the scaling function $r(y)$] for ρ in the vicinity of ρ_c . This analysis in the temporal domain is compatible with the dynamical nature of our simulations and lies at the heart of our calculation of k , x , and the percolation threshold ρ_c . Each trajectory used to calculate the rms displacement δ_{rms} has an identical total dwell time T . We divide this time domain into 16 subintervals and record δ_{rms} at the end of each of these. Ultimately, we average over 50 000 of these trajectories, each associated with statistically independent realizations of disorder, and we do this for nine evenly spaced ρ values centered about and within a few percent of ρ_c .

With a technique described elsewhere [17], we perform the data collapse systematically and objectively by considering a scaling function $r(y) = \sum_{j=1}^n A_j y^j$ (our calculation is converged with respect to n , e.g., with identical results obtained for $n = 5$ and 6) and optimizing with respect to the A_j coefficients via linear least-squares fitting for a given choice of ρ_c , x , and k . We then stochastically vary candidate values for the latter three critical indices until the fit of the analytical scaling to the Monte Carlo data is optimized in a least-squares sense. The main graph in Fig. 5 shows an example of a data collapse generated in this manner. The symbols in the legend correspond to the subinterval times $t_i = iT/16$, where T is the total dwell time.

As an alternative approach, one may also define effective diffusion exponents with $k_{\text{eff}}(t_j, t_i) \equiv \ln[\delta_{\text{rms}}(t_j)/\delta_{\text{rms}}(t_i)]/\ln(t_j/t_i)$ or the secant line for the log-log curve of δ_{rms} over the time interval $[t_i, t_j]$. Percolation thresholds indicated by the crossings are in accord with data collapse results up to the Monte Carlo statistical error. The inset of Fig. 5 displays a crossing of effective diffusion

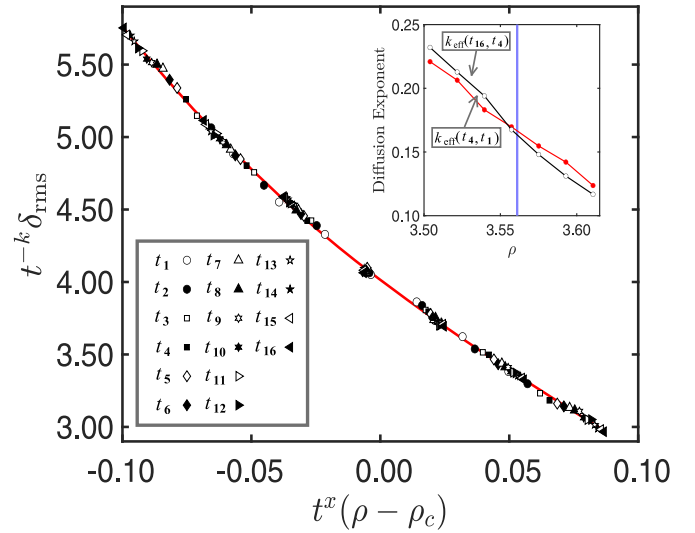


FIG. 5. Sample data collapse for randomly oriented tori of circular cross section for $\tilde{r}_1 = 0.75$. The red line is an analytical curve, while symbols represent Monte Carlo data corresponding to subinterval times $t_i = iT/16$ (T being the total dwell time) as indicated in the legend. The inset shows a crossing of effective diffusion exponents with the vertical blue line indicating ρ_c obtained from a quantitative data collapse.

exponents with the vertical blue line representing the critical concentration gleaned from a quantitative data collapse.

III. RESULTS AND DISCUSSION

A. Percolation thresholds and critical exponents

Unless stated otherwise, critical indices are calculated for dynamical infiltration simulations in which each trajectory involves at least 10^7 collisions with impermeable inclusions. To calculate δ_{rms} , we consider 50 000 trajectories, each of which is associated with a statistically independent realization of disorder. In Fig. 6, ϕ_c results are shown with respect to

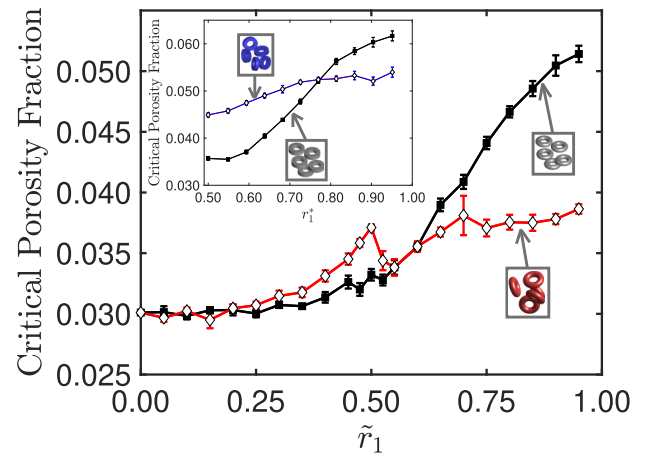


FIG. 6. Critical porosity fractions for aligned (closed squares) and randomly oriented (open diamonds) tori of circular cross section in the main graph and tori of square cross section in the graph inset.

TABLE I. Critical indices for tori with circular cross sections with aligned axes of symmetry.

\tilde{r}_1	ϕ_c	k_{coll}	k_{cross}	x_{coll}
0.05	0.0301(5)	0.18(1)	0.17(1)	0.25(1)
0.10	0.0298(3)	0.16(1)	0.18(1)	0.23(1)
0.15	0.0303(3)	0.18(1)	0.19(1)	0.24(1)
0.20	0.0303(4)	0.18(1)	0.18(1)	0.24(1)
0.25	0.0300(3)	0.16(1)	0.16(1)	0.24(1)
0.30	0.0307(2)	0.18(1)	0.18(1)	0.24(1)
0.35	0.0306(2)	0.17(1)	0.17(1)	0.24(1)
0.40	0.0314(4)	0.18(1)	0.17(1)	0.23(1)
0.45	0.0326(5)	0.20(1)	0.21(1)	0.24(1)
0.475	0.0320(5)	0.16(1)	0.16(1)	0.23(1)
0.50	0.0332(5)	0.17(1)	0.15(1)	0.22(1)
0.525	0.0328(4)	0.17(1)	0.18(1)	0.23(1)
0.55	0.0338(6)	0.18(1)	0.19(1)	0.23(1)
0.60	0.0355(3)	0.16(1)	0.15(1)	0.22(1)
0.65	0.0390(5)	0.19(1)	0.18(1)	0.23(1)
0.70	0.0409(6)	0.16(1)	0.18(1)	0.23(1)
0.75	0.0441(5)	0.18(1)	0.20(1)	0.23(1)
0.80	0.0466(5)	0.18(1)	0.16(1)	0.22(1)
0.85	0.0486(6)	0.18(1)	0.19(1)	0.21(1)
0.90	0.0505(8)	0.21(1)	0.19(1)	0.23(1)
0.95	0.0514(7)	0.20(1)	0.18(1)	0.20(1)

\tilde{r}_1 for aligned and randomly oriented tori. The main graph and inset show results in the case of tori with circular and square cross sections respectively, and critical indices are recorded in Tables I–IV. Closed squares correspond to aligned toroidal grains, while open diamonds represent the randomly oriented counterparts. In the case of tori with circular cross

TABLE II. Critical indices for randomly oriented tori with circular cross sections.

\tilde{r}_1	ϕ_c	k_{coll}	k_{cross}	x_{coll}
0.05	0.0297(3)	0.16(1)	0.16(1)	0.24(1)
0.10	0.0302(3)	0.18(1)	0.17(1)	0.21(1)
0.15	0.0295(7)	0.15(1)	0.18(1)	0.22(1)
0.20	0.0305(3)	0.17(1)	0.18(1)	0.24(1)
0.25	0.0307(3)	0.17(1)	0.16(1)	0.24(1)
0.30	0.0315(4)	0.18(1)	0.19(1)	0.24(1)
0.35	0.0318(4)	0.17(1)	0.18(1)	0.23(1)
0.40	0.0331(5)	0.17(1)	0.18(1)	0.24(1)
0.45	0.0345(5)	0.17(1)	0.15(1)	0.23(1)
0.475	0.0358(1)	0.17(1)	0.16(1)	0.21(1)
0.50	0.0371(3)	0.16(1)	0.16(1)	0.20(1)
0.525	0.0344(8)	0.15(1)	0.15(1)	0.22(1)
0.55	0.0338(7)	0.18(1)	0.19(1)	0.23(1)
0.60	0.0355(4)	0.16(1)	0.15(1)	0.22(1)
0.65	0.0367(4)	0.17(1)	0.16(1)	0.23(1)
0.70	0.0381(16)	0.21(1)	0.18(1)	0.22(1)
0.75	0.0371(7)	0.17(1)	0.17(1)	0.20(1)
0.80	0.0376(6)	0.17(1)	0.19(1)	0.22(1)
0.85	0.0375(7)	0.17(1)	0.16(1)	0.21(1)
0.90	0.0378(4)	0.17(1)	0.18(1)	0.21(1)
0.95	0.0386(4)	0.19(1)	0.21(1)	0.21(1)

TABLE III. Critical indices for tori with square cross sections and aligned axes of symmetry.

r_1^*	ϕ_c	k_{coll}	k_{cross}	x_{coll}
$1/\sqrt{5}$	0.0357(4)	0.17(1)	0.18(1)	0.24(1)
0.50	0.0355(3)	0.18(1)	0.18(1)	0.26(1)
0.55	0.0371(4)	0.18(1)	0.18(1)	0.25(1)
0.60	0.0404(5)	0.20(1)	0.20(1)	0.25(1)
0.65	0.0439(2)	0.18(1)	0.17(1)	0.25(1)
0.70	0.0478(5)	0.18(1)	0.20(1)	0.24(1)
0.75	0.0521(5)	0.18(1)	0.18(1)	0.23(1)
0.80	0.0563(7)	0.20(1)	0.20(1)	0.23(1)
0.85	0.0584(7)	0.18(1)	0.20(1)	0.23(1)
0.90	0.0603(10)	0.18(1)	0.20(1)	0.23(1)
0.95	0.0617(11)	0.18(1)	0.19(1)	0.22(1)

sections, a prominent cusp in the ϕ_c curve is evident for randomly oriented inclusions for $\tilde{r}_1 = 0.5$, coinciding with the topological transition marked by the emergence of a central hole with increasing \tilde{r}_1 . For $\tilde{r}_1 > 0.5$, the critical porosity drops sharply before gradually rising, appearing to saturate at $\phi_c = 0.038(1)$. The cusp feature is either significantly muted or absent for the aligned counterparts.

The appearance of a central hole for $\tilde{r}_1 = 0.5$ as cone-shaped dimples above and below the equatorial plane merge suggests an explanation for the ϕ_c cusp in the case of randomly oriented grains with circular cross section. The sharp increase in ϕ_c as one approaches $\tilde{r}_1 = 0.5$ from the left is consistent with the upper and lower concave depressions being sheltered pockets of space, which enhances the critical porosity fraction. On the other hand, immediately to the right of the $\tilde{r} = 0.5$ boundary, the incipient central hole serves as a channel uniting the upper and lower voids, abruptly enhancing the overall permeability of the system and hence accounting for the sudden drop in ϕ_c with increasing \tilde{r}_1 .

The critical porosity fraction for aligned tori with circular cross sections does not exhibit a prominent cusp as in the case of the randomly oriented counterparts. In addition, as \tilde{r}_1 increases toward unity (i.e., in the regime of ringlike or high-aspect-ratio grains), ϕ_c for aligned toroidal inclusions ultimately saturates at a markedly higher porosity fraction

TABLE IV. Critical indices for randomly oriented tori with square cross sections.

r_1^*	ϕ_c	k_{coll}	k_{cross}	x_{coll}
$1/\sqrt{5}$	0.0449(4)	0.16(1)	0.17(1)	0.21(1)
0.50	0.0458(4)	0.17(1)	0.17(1)	0.23(1)
0.55	0.0475(5)	0.17(1)	0.18(1)	0.22(1)
0.60	0.0490(5)	0.17(1)	0.17(1)	0.22(1)
0.65	0.0504(8)	0.17(1)	0.15(1)	0.21(1)
0.70	0.0519(4)	0.19(1)	0.20(1)	0.23(1)
0.75	0.0524(5)	0.18(1)	0.18(1)	0.22(1)
0.80	0.0526(6)	0.18(1)	0.18(1)	0.22(1)
0.85	0.0533(9)	0.16(1)	0.19(1)	0.20(1)
0.90	0.0521(9)	0.16(1)	0.16(1)	0.20(1)
0.95	0.0540(11)	0.19(1)	0.17(1)	0.21(1)

TABLE V. Critical indices for square prisms with axes of symmetry aligned.

Aspect ratio	ϕ_c	k_{coll}	k_{cross}	x_{coll}
1	0.0380(3)	0.19(1)	0.17(1)	0.25(1)
3/2	0.0379(2)	0.19(1)	0.19(1)	0.26(1)
2	0.0379(5)	0.19(1)	0.19(1)	0.25(1)
5/2	0.0379(5)	0.19(1)	0.18(1)	0.26(1)
3	0.0378(4)	0.19(1)	0.21(1)	0.27(1)
4	0.0377(5)	0.19(1)	0.19(1)	0.25(1)
5	0.0379(5)	0.19(1)	0.20(1)	0.26(1)
6	0.0375(5)	0.18(1)	0.18(1)	0.27(1)
7	0.0381(3)	0.20(1)	0.18(1)	0.27(1)
8	0.0381(6)	0.20(1)	0.18(1)	0.28(1)

than for randomly oriented tori. A possible explanation for both the absence of a cusp at the topological transition and convergence to a higher ϕ_c as aligned tori become ringlike is the tendency of neighbors above and below to shield the cone-shaped dimples or central hole for $\tilde{r}_1 < 1/2$ and $\tilde{r}_1 > 1/2$, respectively, thereby offsetting the potential enhancement to overall permeability offered by the emergence of a conduit through the grain. Similar reasoning may also explain why ϕ_c for aligned grains exceeds that of randomly oriented counterparts in the high-aspect-ratio regime; again, the alignment of the axes of symmetry of the tori may increase the likelihood of the grain's central hole being closed off from connected void spaces, favoring a lower critical concentration than for the randomly oriented counterparts.

The inset of Fig. 6 shows critical porosities in the case of toroidal grains with a square cross section with open diamonds and filled squares representing ϕ_c results for randomly oriented and aligned inclusions, respectively. For r_1^* in the vicinity of $1/\sqrt{5}$ with an incipient cylindrical central channel, ϕ_c for systems made up of aligned grains exceeds that of media comprised of randomly oriented grains. However, this ordering is reversed with increasing r_1^* with a crossing in the ϕ_c curves near $r_1^* = 0.75$. Ultimately, the critical porosity fraction saturates beyond 0.060 if the impermeable inclusions are aligned and near 0.053(2) for randomly oriented grains.

In contrast to the case of tori of circular cross section, there is no cusp feature for either aligned or randomly oriented grains of square cross section. The absence of a sharp decrease in ϕ_c with increasing r_1^* may be due to the abrupt appearance of a central hole with no cone-shaped indentations above or below the equatorial plane. In the absence of these void pockets the emerging central channels thus have a significantly diminished role in expanding navigable connected volume networks.

As \tilde{r}_1 and r_1^* approach unity with ringlike shapes for tori of circular and square cross sections, one also attains the high-aspect-ratio regime where small segments of toroidal grains resemble the linear counterparts, cylinders and square prisms, respectively. Although percolation thresholds for aligned and randomly oriented cylinders have been previously calculated [18], in this work we calculate critical indices for elongated (noncubic) square prism shaped grains; results for a variety of aspect ratios r_A appear in Tables V and VI with ϕ_c displayed

TABLE VI. Critical indices for randomly oriented square prisms.

Aspect ratio	ϕ_c	k_{coll}	k_{cross}	x_{coll}
1	0.0449(5)	0.17(1)	0.19(1)	0.23(1)
3/2	0.0461(14)	0.18(1)	0.21(1)	0.23(1)
2	0.0465(7)	0.16(1)	0.17(1)	0.22(1)
5/2	0.0483(8)	0.16(1)	0.17(1)	0.22(1)
3	0.0485(11)	0.18(1)	0.19(1)	0.22(1)
4	0.0505(7)	0.19(1)	0.19(1)	0.24(1)
5	0.0515(7)	0.17(1)	0.19(1)	0.22(1)
6	0.0519(5)	0.17(1)	0.18(1)	0.23(1)
7	0.0519(3)	0.17(1)	0.18(1)	0.23(1)
8	0.0523(6)	0.18(1)	0.18(1)	0.22(1)
10	0.0524(5)	0.17(1)	0.17(1)	0.22(1)
15	0.0535(4)	0.19(1)	0.19(1)	0.23(1)
20	0.0534(4)	0.16(1)	0.15(1)	0.23(1)

in the graph in Fig. 7. Closed squares and open diamonds represent aligned and randomly oriented grains, respectively. While ϕ_c in the case of randomly oriented grains increases monotonically with r_A , ultimately saturating in the vicinity of 0.052(5), the critical porosity fraction for aligned counterparts appears (at least up to Monte Carlo error) to be constant at 0.0379(5) (the dashed horizontal line indicates this mean value) with respect to the aspect ratio (for a significant range of r_A values) of prism-shaped inclusions. The markedly lower ϕ_c values for the aligned case may be due to the presence of channels flanked and sheltered by parallel rectangular facets, uninterrupted void conduits which tend to be disrupted in the case of randomly oriented square prisms.

Among toroidal grains and linear counterparts of both circular and square cross sections, as is evident in Figs. 8(b) and 8(d), the critical porosity fractions for randomly oriented toroidal grains and corresponding ϕ_c results for linear inclusions converge. On the other hand, as may be seen in Figs. 8(a) and 8(c), for aligned inclusions critical porosity fractions are smaller for toroidal grains than for linear counterparts in the small-aspect-ratio regime where the tori have a more compact structure. However, the ϕ_c curves cross for $r_A \sim 1$ with the critical porosities for tori rising monotonically and eventually saturating at a significantly higher value than for the linear

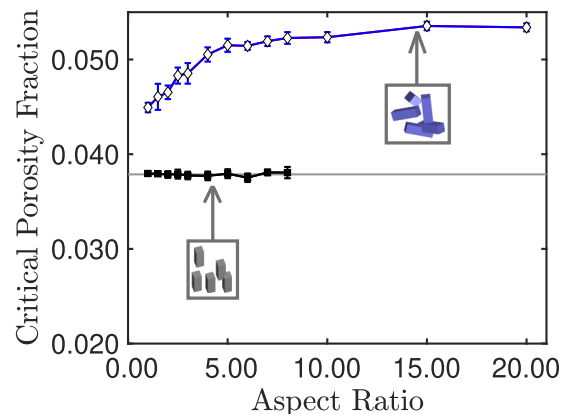


FIG. 7. Critical porosity fractions for aligned (closed squares) and rotated (open diamonds) square prisms.

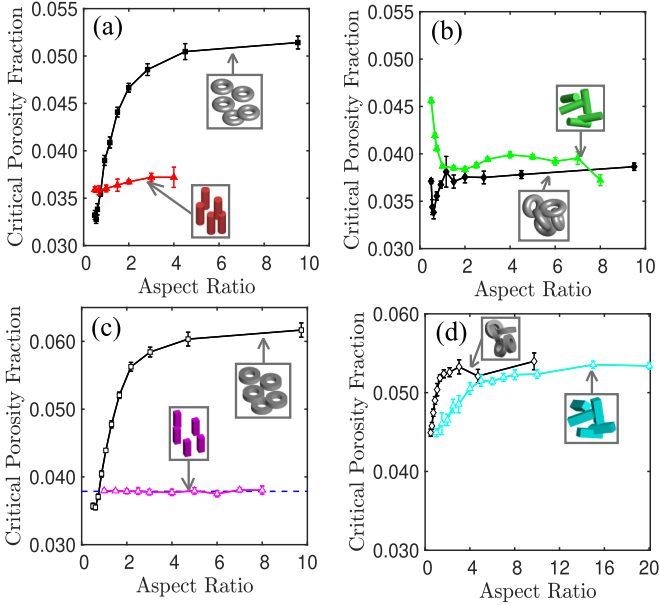


FIG. 8. Critical porosity fraction versus aspect ratio for (a) aligned tori of circular cross section and cylinders, (b) randomly oriented tori of circular cross section and cylinders, (c) aligned tori of square cross section and square prisms, and (d) randomly oriented tori of square cross section and square prisms.

counterparts. The variation of the orientation of small quasi-linear segments of ringlike tori in the equatorial plane likely disrupts long narrow channels which remain intact for aligned cylinders and prisms in the high-aspect-ratio regime, thereby elevating ϕ_c for aligned tori.

B. Validation of dynamical infiltration simulations

We have checked to see that our results are converged with respect to the lengths of the dynamical infiltration trajectories. In this vein, we have conducted studies in which virtual tracers interact with constituent impermeable grains a mean of 10^6 times (i.e., short runs) with constituent grains for the sake of comparison with results gleaned for dwell times an order of magnitude longer (referred to here as long runs) with at least on average 10^7 collisions of tracers with impermeable inclusions. As in the case of the results mentioned in the context of the longer runs, critical indices obtained in the case of the shorter runs involve averaging over 50 000 distinct trajectories corresponding to statistically independent realizations of disorder. We consider the results of short and long runs in juxtaposition to check on convergence with respect to the trajectory dwell time. The graphs in Fig. 9 display ratios of ρ_c gleaned from long runs to the critical concentration calculated from short runs for each geometry considered in this work. In general, the ratios are consistent with unity (indicated by dashed horizontal lines) up to Monte Carlo statistical error.

Dynamical exponent ratios k/x are plotted in the graphs in Fig. 10 for each grain geometry considered in this work with circles and squares indicating long and short run results, respectively; again, Figs. 10(a), 10(c), and 10(e) pertain to aligned grains, while Figs. 10(b), 10(d), and 10(f) correspond to randomly oriented inclusions. The dashed horizontal lines

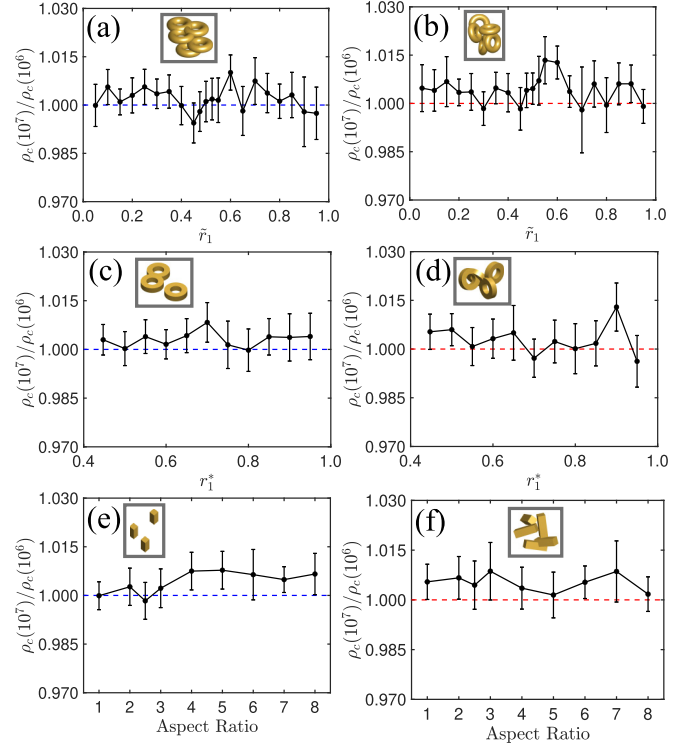


FIG. 9. Critical concentration ratios for calculations with 10^7 and 10^6 interactions of virtual tracer particles with grains (a), (c), and (e) aligned and (b), (d), and (f) randomly oriented. Results are shown for (a) and (b) tori of circular cross section, (c) and (d) tori of square cross section, and (e) and (f) square prisms.

indicate the 0.667 exponent ratio obtained from universal scaling arguments. With trajectories encompassing an order of magnitude more interactions with impermeable grains, k/x results are generally in closer agreement with the universal scaling result. Based on this trend, one may surmise that increasing the dwell time even further would yield k/x results in even closer accord with the 0.667 line. Nevertheless, as may be seen in Fig. 9, critical porosities ϕ_c are converged with respect to the dynamical infiltration trajectory dwell time.

IV. CONCLUSION

We have examined percolation phenomena for nonconvex impermeable grains in the form of toroidal shapes of circular and square cross sections. In the case of the former, when tori with circular cross section (or indeed, we expect, with any concavity above and below the axis of symmetry) are randomly oriented, the topological transition signaled by the appearance of a central hole is also marked by a cusp in the critical porosity fraction with incipient central holes acting as channels to expand the network of void volumes. We found convergence and saturation at a common value of ϕ_c for the randomly oriented tori and linear counterparts in the high-aspect-ratio limit where cross-sectional length scales are dwarfed by the central hole radius; however, this convergence in the critical porosity fractions does not occur among tori and linear counterparts in the case in which the grain axes of symmetry are aligned. We also have calculated critical

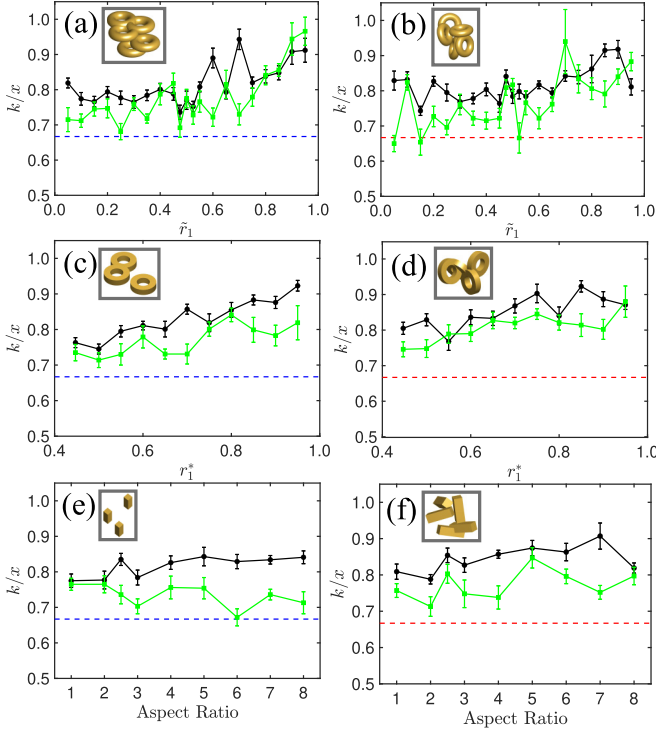


FIG. 10. Exponent ratios k/x with black closed circles and green closed squares corresponding to calculations for 10^7 and 10^6 interactions of virtual tracer particles with (a), (c), and (e) aligned grains and (b), (d), and (f) randomly oriented inclusions. Results are shown for tori of (a) and (b) circular cross section, (c) and (d) square cross section, and (e) and (f) square prisms. Dashed horizontal lines indicate the 0.667 ratio based on universal scaling arguments.

porosity fractions for square prisms for a wide range of aspect ratios in the randomly oriented and aligned cases, finding no variation in ϕ_c across this broad r_A range.

We have achieved significant gains in computational efficiency by implementing an approach in which voxels occupied by virtual tracers as well as neighboring cells are populated with grains, which allows rescaling the inclusions relative to voxels, thereby altering the mean number of grains overlapping cubic cells. In this manner, with an optimal choice of the inclusion dilation factor, the computational burden remains essentially constant even in the high-aspect-ratio regime. The improvements in computational efficiency have permitted an increase in trajectory dwell times by an order of magnitude, yielding tracer paths involving an average of 10^7 collisions but with the same critical porosity fraction results as in the case of the shorter runs, up to Monte Carlo statistical error.

ACKNOWLEDGMENTS

We acknowledge helpful discussions with Michael Crescimanno. Calculations in this work have benefited from use of the Ohio Supercomputing Center, OSC [26].

APPENDIX

Toroidal grains of circular cross section are characterized by the orientation unit vector \hat{u} of the axis of symmetry, their location \vec{x} , and the major and minor axes r_1 and r_2 with the former being the radius of revolution and the latter the cross section radius. It is convenient to operate in terms of the tracer particle position relative to the torus geometric center $\vec{\Delta} \equiv \vec{x} - \vec{x}_c$, where $\vec{x} = \vec{x}_0 + \hat{v}t$ in seeking the time t for the virtual tracer particle to intersect with the toroidal surface. The vector $\vec{v}_{\text{plane}} \equiv r_1[\vec{\Delta} - (\vec{\Delta} \cdot \hat{u})\hat{u}]/\sqrt{\Delta^2 - (\vec{\Delta} \cdot \hat{u})^2}$ is aligned with the projection of $\vec{\Delta}$ onto the equatorial plane of the torus and is on the circle of radius r_1 , the locus of centers of circles of revolution. For an intersection with the surface of the grain, one insists that $|\vec{\Delta} - \vec{v}_{\text{plane}}| = r_2$. Squaring both sides, isolating and squaring the radical expression, and inserting $\vec{\Delta} = \vec{\Delta}_0 + \hat{v}t$ (where $\vec{\Delta}_0 \equiv \vec{x}_0 - \vec{x}_c$) yields a quartic equation in t :

$$t^4 + 4(\vec{\Delta}_0 \cdot \hat{v})t^3 + [4(\vec{\Delta}_0 \cdot \hat{v})^2 + 4\Delta_0^2 - 2(r_1^2 + r_2)^2 + 2r_1^2(\hat{v} \cdot \hat{u})^2]t^2 + [4\Delta_0^2(\vec{\Delta}_0 \cdot \hat{v}) - 4(\vec{\Delta}_0 \cdot \hat{v})(r_1^2 + r_2^2) + 8(\hat{v} \cdot \hat{u})(\vec{\Delta}_0 \cdot \hat{u})r_1^2]t + [\Delta_0^2 + (r_1^2 - r_2^2)]^2 = 0. \quad (\text{A1})$$

The roots may be found analytically [27], and for a computationally robust approach we introduce a shift in t to eliminate the linear term in Eq. (1) and then factor the resulting depressed quartic into two readily soluble quadratic equations. Fortunately, this factorization involves solving a cubic equation, which always has at least one real root.

As in the case of tori with square cross sections, care must be taken if a virtual tracer interacts with the same grain more than once in succession. In such a situation, factoring out the zero root yields a cubic equation, which also is amenable to exact solution. Disposing of the zero root (whose physical meaning is that the tracer particle has not left the surface) in this manner avoids its confusion with a scattering event due to limits on numerical precision. When the nearest intersection point $\vec{\Delta}$ has been identified, one then obtains the surface normal, given by $\hat{n} = \vec{v}_{\perp}/r_2$, where the locally perpendicular direction is $\vec{v}_{\perp} = \vec{\Delta} - \vec{v}_{\text{plane}}$.

- [1] D. Stauffer and A. Aharony, *Introduction to Percolation Theory*, 2nd ed. (Taylor & Francis, Bristol, 1994).
- [2] J. Hoshen and R. Kopelman, *Phys. Rev. B* **14**, 3438 (1976).
- [3] W. T. Elam, A. R. Kerstein, and J. J. Rehr, *Phys. Rev. Lett.* **52**, 1516 (1984).
- [4] S. C. van der Marck, *Phys. Rev. Lett.* **77**, 1785 (1996).
- [5] M. D. Rintoul, *Phys. Rev. E* **62**, 68 (2000).

- [6] M. A. Klatt, R. M. Ziff, and S. Torquato, *Phys. Rev. E* **104**, 014127 (2021).
- [7] N. S. Martys, S. Torquato, and D. P. Bentz, *Phys. Rev. E* **50**, 403 (1994).
- [8] R. S. Maier, D. M. Kroll, H. T. Davis, and R. S. Bernard, *J. Colloid Interface Sci.* **217**, 341 (1999).
- [9] Y. B. Yi, *Phys. Rev. E* **74**, 031112 (2006).

- [10] Y. B. Yi and K. Esmail, *J. Appl. Phys.* **111**, 124903 (2012).
- [11] Z. Koza, G. Kondrat, and K. Suszcyński, *J. Stat. Mech.* (2014) P11005.
- [12] F. Höfling, T. Munk, E. Frey, and T. Franosch, *J. Chem. Phys.* **128**, 164517 (2008).
- [13] M. Spanner, F. Höfling, S. C. Kapfer, K. R. Mecke, G. E. Schröder-Turk, and T. Franosch, *Phys. Rev. Lett.* **116**, 060601 (2016).
- [14] F. Höfling, T. Franosch, and E. Frey, *Phys. Rev. Lett.* **96**, 165901 (2006).
- [15] A. Kammerer, F. Höfling, and T. Franosch, *Europhys. Lett.* **84**, 66002 (2008).
- [16] M. Spanner, F. Höfling, G. E. Schröder-Turk, K. Mecke, and T. Franosch, *J. Phys.: Condens. Matter* **23**, 234120 (2011).
- [17] D. J. Priour, Jr., *Phys. Rev. E* **89**, 012148 (2014).
- [18] D. J. Priour and N. J. McGuigan, *Phys. Rev. Lett.* **121**, 225701 (2018).
- [19] H. A. Lorentz, *Proc. R. Acad. Amst.* **7**, 438 (1905).
- [20] C. Bruin, *Physica* **72**, 261 (1974).
- [21] H. van Beijeren, *Rev. Mod. Phys.* **54**, 195 (1982).
- [22] T. Bauer, F. Höfling, T. Munk, E. Frey, and T. Franosch, *Eur. Phys. J. Spec. Top.* **189**, 103 (2010).
- [23] D. ben-Avraham and S. Havlin, *Diffusion and Reactions in Fractals and Disordered Systems* (Cambridge University Press, Cambridge, 2000).
- [24] J. Wang, Z. Zhou, W. Zhang, T. M. Garoni, and Y. Deng, *Phys. Rev. E* **87**, 052107 (2013).
- [25] B. Kozlov and M. Lagnuës, *Physica A* **389**, 5339 (2010).
- [26] Ohio Supercomputer Center. 1987. Ohio Supercomputer Center. Columbus OH Ohio Supercomputer Center. <http://osc.edu/ark/19495/f5s1ph73>.
- [27] S. Neumark, *Solution of Cubic and Quartic Equations* (Pergamon, New York, 1965).